CHEMISTRY OF MATERIALS
Article

Chem. Mater. **2009,** *21,* 2825–2834 2825
DOI:10.1021/cm9004486

Microwave Synthesis of Bimetallic Nanoalloys and CO Oxidation on Ceria-Supported Nanoalloys

Victor Abdelsayed, Ahlam Aljarash, and M. Samy El-Shall*

Department of Chemistry, Virginia Commonwealth University, Richmond, Virginia 23284-2006

Zeid A. Al Othman and Ahmed H. Alghamdi

Department of Chemistry, King Saud University, Riyadh 11541, Saudi Arabia

Received February 14, 2009. Revised Manuscript Received April 23, 2009

A facile and fast microwave irradiation (MWI) method has been developed to prepare a wide variety of pure metallic and bimetallic alloy nanoparticles with controlled size and shape. The important advantage of microwave dielectric heating over convective heating is that the reactants can be added at room temperature (or slightly higher temperatures) without the need for high-temperature injection. The method allows the passivation of the nanocrystals by using a mixture of olyel amine and oleic acid as a solvent, a reducing agent, and a capping material. We investigate the controlled synthesis of nanoalloys among the nanocrystals of Au, Ag, Pt, Pd, Ru, Rh, Cu, and Ni by studying the changes in the structural and optical properties of the resulting nanoalloys with respect to the individual metals. Using the same method, we also report the synthesis of selected nanoalloys supported on ceria nanoparticles as nanocatalysts for CO oxidation. The catalytic activities for CO oxidation are presented and discussed. High activity and thermal stability have been observed for the nanoalloys according to the order CuPd > CuRh > AuPd > AuRh > PtRh > PdRh > AuPt. The method could be applied for the synthesis of multimetallic nanoalloys with novel properties resulting from the different metallic properties coupled together in a single nanoalloy.

Introduction

Considerable research interest has been focused on the study of bimetallic nanoalloys due to the additional new properties that may arise from the combination of different compositions of metals on the nanoscale.[1−37] At a fundamental level, information on the evolution of the electronic

*To whom correspondence should be addressed. E-mail: mselshal@vcu.edu.

(1) Nanoalloys: From theory to applications. Faraday Discuss. 2008, 138.
(2) Thomas, J. M.; Adams, R. D.; Boswell, E. M.; Captain, B.; Grönbeck, H.; Raja, R. *Faraday Discuss.* **2008**, *138*, 301–315.
(3) Jellinek, J. *Faraday Discuss.* **2008**, *138*, 11–35.
(4) Abdelsayed, V.; Glaspell, G.; Nguyen, M.; Howe, J. M.; El-Shall, M. S. *Faraday Discuss.* **2008**, *138*, 163–180.
(5) Park Jeong, Y.; Zhang, Y.; Grass, M.; Zhang, T.; Somorjai Gabor, A. *Nano Lett.* **2008**, *8*, 673–677.
(6) Glaspell, G.; Hassan, H. M. A.; Elzatahry, A.; Abdalsayed, V.; El-Shall, M. S. *Top. Catal.* **2008**, *47*, 22–31.
(7) Habas, S. E.; Lee, H.; Radmilovic, V.; Somorjai, G. A.; Yang, P. *Nat. Mater.* **2007**, *6*, 692–697.
(8) Hernandez, J.; Solla-Gullon, J.; Herrero, E.; Aldaz, A.; Feliu, J. M. *J. Phys. Chem. C* **2007**, *111*, 14078–14083.
(9) Koh, S.; Strasser, P. *J. Am. Chem. Soc.* **2007**, *129*, 12624–12625.
(10) Harada, M.; Einaga, H. *J. Colloid Interface Sci.* **2007**, *308*, 568–572.
(11) Li, H.; Sun, G.; Li, N.; Sun, S.; Su, D.; Xin, Q. *J. Phys. Chem. C* **2007**, *111*, 5605–5617.
(12) Nitani, H.; Nakagawa, T.; Daimon, H.; Kurobe, Y.; Ono, T.; Honda, Y.; Koizumi, A.; Seino, S.; Yamamoto, T. *Appl. Catal.* **2007**, *326*, 194–201.
(13) Santiago, E. I.; Varanda, L. C.; Villullas, H. M. *J. Phys. Chem. C* **2007**, *111*, 3146–3151.
(14) Sun, Y.; Zhang, L.; Zhou, H.; Zhu, Y.; Sutter, E.; Ji, Y.; Rafailovich, M. H.; Sokolov, J. C. *Chem. Mater.* **2007**, *19*, 2065–2070.
(15) Wang, C.; Daimon, H.; Lee, Y.; Kim, J.; Sun, S. *J. Am. Chem. Soc.* **2007**, *129*, 6974–6975.
(16) Samia, A. C. S.; Schlueter, J. A.; Jiang, J. S.; Bader, S. D.; Qin, C.-J.; Lin, X.-M. *Chem. Mater.* **2006**, *18*, 5203–5212.
(17) Agrawal, V. V.; Mahalakshmi, P.; Kulkarni, G. U.; Rao, C. N. R. *Langmuir* **2006**, *22*, 1846–1851.
(18) Sun, S. *Adv. Mater.* **2006**, *18*, 393–403.
(19) Rutledge, R. D.; Morris, W. H.; Wellons, M. S.; Gai, Z.; Shen, J.; Bentley, J.; Wittig, J. E.; Lukehart, C. M. *J. Am. Chem. Soc.* **2006**, *128*, 14210–14211.
(20) Abdelsayed, V.; Saoud, K. M.; El-Shall, M. S. *J. Nanopart. Res.* **2006**, *8*, 519–531.
(21) Glaspell, G.; Abdelsayed, V.; Saoud, K. M.; El-Shall, M. S. *Pure Appl. Chem.* **2006**, *78*, 1667–1689.
(22) Peng, Z.; Spliethoff, B.; Tesche, B.; Walther, T.; Kleinermanns, K. *J. Phys. Chem. B* **2006**, *110*, 2549–2554.
(23) Smetana, A. B.; Klabunde, K. J.; Sorensen, C. M.; Ponce, A. A.; Mwale, B. *J. Phys. Chem. B* **2006**, *110*, 2155–2158.
(24) Yang, Y.; Saoud, K. M.; Abdelsayed, V.; Glaspell, G.; Deevi, S.; El-Shall, M. S. *Catal. Commun.* **2006**, *7*, 281–284.
(25) Zhou, G.; Lu, M.; Yang, Z. *Langmuir* **2006**, *22*, 5900–5903.
(26) Liu, Z.; Ada, E. T.; Shamsuzzoha, M.; Thompson, G. B.; Nikles, D. E. *Chem. Mater.* **2006**, *18*, 4946–4951.
(27) Huang, J.; Liu, Z.; He, C.; Gan, L. M. *J. Phys. Chem. B* **2005**, *109*, 16644–16649.
(28) Chen, M.; Liu, J. P.; Sun, S. *J. Am. Chem. Soc.* **2004**, *126*, 8394–8395.
(29) Liu, Z.; Ling, X. Y.; Su, X.; Lee, J. Y. *J. Phys. Chem. B* **2004**, *108*, 8234–8240.
(30) Sra, A. K.; Schaak, R. E. *J. Am. Chem. Soc.* **2004**, *126*, 6667–6672.
(31) Mandal, M.; Kundu, S.; Sau, T. K.; Yusuf, S. M.; Pal, T. *Chem. Mater.* **2003**, *15*, 3710–3715.
(32) Moore, J. T.; Corn, J. D.; Chu, D.; Jiang, R.; Boxall, D. L.; Kenik, E. A.; Lukehart, C. M. *Chem. Mater.* **2003**, *15*, 3320–3325.
(33) Worley, Z. J.; Denommee, S.; Kingston, C.; Jakubek, Z. J.; Deslandes, Y.; Post, M.; Simard, B.; Braidy, N.; Botton, G. A. *J. Phys. Chem. B* **2003**, *107*, 6920–6923.
(34) Park, K.; Choi, J.; Kwon, B.; Lee, S.; Sung, Y.; Ha, H.; Hong, S.; Kim, H.; Weickowski, A. A. *J. Phys. Chem. B* **2002**, *106*, 1869–1877.
(35) Chen, Y.-H.; Yeh, C.-S. *Chem. Commun.* **2001**, 371–372.
(36) Link, S.; Burda, C.; Nikoobakht, B.; El-Sayed, M. A. *J. Phys. Chem. B* **2000**, *104*, 6152–6163.
(37) Sun, S.; Murray, C. B.; Weller, D.; Folks, L.; Moser, A. *Science* **2000**, *287*, 1989–1992.

Published on Web 05/26/2009

structures of bimetallic nanoparticles as a function of size, composition, and shape and the associated changes in the optical, catalytic, and magnetic properties continues to be a major goal of research in nanostructured materials. On a practical level, the unique properties of metallic and bimetallic nanoparticles are exploited for a variety of applications including nanocatalysis particularly for efficient selective catalysts, sensors, optical markers, and filters, fuel and oil additives for energy enhancement and surface modifications, and many other applications. The applications of nanoparticle alloys are thus expected to enhance many fields of advanced materials and relevant technology particularly in the areas of catalysis, chemical and biological sensors, optoelectronics, drug delivery, and media storage.

Several methods based on physical and chemical approaches have been developed for the synthesis of controlled size and shape nanostructures including nanoalloys. Examples of these approaches include solvothermal methods, template-assisted, kinetic growth control, sonochemical reactions, and thermolysis of single-source precursors in ligating solvents.[38−47] Most of the reported methods involve high temperature (∼300 °C) decomposition of the metal precursor and require rigorous inert environments. The requirements of high temperature and inert atmosphere limit the large-scale production of the nanoalloys, and there is a need to develop general and simple synthetic methods operative at near room temperature in air and applicable to a wide range of nanoalloy systems.

Recently, we developed a new approach based on microwave irradiation (MWI) for the synthesis of a variety of high quality, nearly monodisperse nanoparticles at low temperatures.[45−48] The MWI approach provides simple and fast routes to the synthesis of nanomaterials since no high temperature or high pressure is needed. Furthermore, MWI is particularly useful for a controlled large-scale synthesis that minimizes the thermal gradient effects.[49−62] As a result of the difference in the solvent and reactant dielectric constants, selective dielectric heating can provide significant enhancement in reaction rates. The rapid transfer of energy directly to the reactants (faster than they are able to relax) causes an instantaneous internal temperature rise. By using metal precursors that have large microwave absorption cross sections relative to the solvent, very high effective reaction temperatures can be achieved. This allows the rapid decomposition of the precursors thus creating highly supersaturated solutions where nucleation and growth can take place to produce the desired nanocrystalline products. These conditions lead to the formation of very small nanocrystals since the higher the supersaturation the smaller the critical size required for nucleation.[48] For the formation of nanoalloys, the experimental conditions must be chosen to yield binary nucleation events where the initial nuclei contain both metals with compositions that reflect the compositions of the two metal precursors. This requires careful choice of the two metal precursors with almost identical decomposition profiles to ensure the occurrence of binary nucleation events. These conditions are different from those involved in the formation of core−shell nanoparticles, where the shell atoms heterogeneously nucleate on the pre-existing core nuclei. Following the nucleation events, the growth of the nanoalloy nanocrystals can be effectively inhibited by the adsorption of ligating organic surfactants that bind strongly to the nanocrystals, thus stabilizing and passivating the surface. In nanoalloys, depending on the surface composition of the binary nanocrystal faces, selective adsorption of the capping agents can result in controlling the final shape of the grown nanocrystal. Since in MWI it is possible to quench the reaction very early on (∼10 s), this provides the opportunity of controlling the nanostructures from small spherical nuclei to short rods to extended assemblies of nanowires by varying the MWI reaction time, the composition of the nanoalloy, and the type and concentration of different capping agents that exhibit variable binding strengths to the metals in the nanocrystal.[45−48]

One of the important applications of metallic and bimetallic nanocrystals is in the area of nanocatalysis. Nanocatalysis is a phenomenon of significant fundamental research and important practical applications in a variety of fields such as chemistry, physics, materials, and environmental and atmospheric sciences in addition to

(38) Park, S.; Joo, J.; Kwon, S. G.; Jang, Y.; Hyeon, T. *Angew. Chem., Int. Ed.* **2007**, *46*, 4630–4660.
(39) Nanoparticles from Theory to Application, Schmidt, G., Ed.; Wiley-VCH: Weinheim, 2004.
(40) Alivisatos, A. P. *J. Phys. Chem.* **1996**, *100*, 13226–13239.
(41) Peng, Z.; Manna, W.; Wickham, J.; Scher, E.; Kadavanich, A.; Alivisatos, A. P. *Nature* **2000**, *404*, 59–61.
(42) Park, J.; An, K.; Hwang, Y.; Park, J.-G.; Noh, H.-J.; Kim, J.-Y.; Park, J.-H.; Hwang, N.-M.; Hyeon, T. *Nat. Mater.* **2004**, *3*, 891–895.
(43) Li, Y.; Malik, M. A.; O'Brien, P. *J. Am. Chem. Soc.* **2005**, *127*, 16020–16021.
(44) Wang, X.; Zhuang, J.; Peng, Q.; Li, Y. *Nature* **2005**, *437*, 121–124.
(45) Glaspell, G.; Fuoco, L.; El-Shall, M. S. *J. Phys. Chem. B* **2005**, *109*, 17350–17355.
(46) Panda, A. B.; Glaspell, G. P.; El-Shall, M. S. *J. Am. Chem. Soc.* **2006**, *128*, 2790–2791.
(47) Panda, A. B.; Glaspell, G. P.; El-Shall, M. S. *J. Phys. Chem. C* **2007**, *111*, 1861–1864.
(48) Abdelsayed, V.; Panda, A. B.; Glaspell, G. P.; El-Shall, M. S. In Nanoparticles: Synthesis, Stabilization, Passivation, and Functionalization; ACS Symposium Series 996; Nagarajan, R., Hatton, T. A., Eds.; American Chemical Society: Washington, DC, 2008; Chapter 17, pp 225−247.
(49) Zhu, J.; Palchik, O.; Chen, S.; Gedankan, A. *J. Phys. Chem. B* **2000**, *104*, 7344–7347.
(50) Murgan, A. V.; Sonawane, R. S.; Kale, B. B.; Apte, S. K.; Kulkarni, A. V. *Mater. Chem. Phys.* **2001**, *71*, 98–102.
(51) Gallis, K.; Landry, C. *Adv. Mater.* **2001**, *13*, 23–26.
(52) Boxall, D.; Deluga, G. A.; Kenik, E. A.; King, W. D.; Lukehart, C. *Chem. Mater.* **2001**, *13*, 891–900.
(53) Liang, J.; Deng, Z. X.; Jiang, X.; Li, F.; Li, Y. *Inorg. Chem.* **2002**, *41*, 3602–3604.
(54) He, J.; Zhao, X. N.; Zhu, J. J.; Wang, J. *J. Cryst. Growth* **2002**, *240*, 389–394.
(55) Pastoriza-Santos, I.; Liz-Marzán, L. *Langmuir* **2002**, *18*, 2888–2894.
(56) Chen, D.; Tang, K.; Shen, G.; Sheng, J.; Fang, Z.; Liu, X.; Zheng, H.; Qian, Y. *Mater. Chem. Phys.* **2003**, *82*, 206–209.
(57) Lu, Q.; Gao, F.; Komarneni, S. *J. Mater. Res.* **2004**, *19*, 1649–1655.
(58) Harpeness, R.; Gedanken, A. *Langmuir* **2004**, *20*, 3431–3434.
(59) Chen, W.; Zhao, J.; Lee, J. Y.; Liu, Z. *Mater. Chem. Phys.* **2005**, *91*, 124–129.
(60) Gerbec, J. A; Magana, D.; Washington, A.; Strouse, G. F. *J. Am. Chem. Soc.* **2005**, *127*, 15791–15800.
(61) Patra, C. R.; Alexandra, G.; Patra, S.; Jacob, D. S.; Gedanken, A.; Landau, A.; Gofer, Y. *New J. Chem.* **2005**, *29*, 733–739.
(62) Tsuji, M.; Hashimoto, M.; Nishizawa, Y.; Kubokawa, M.; Tsuji, T. *Chem.—Eur. J.* **2005**, *11*, 440–452.

its traditional significance in advancing the petroleum field.[5−9,11,12,20,21,24,63−70]

Metallic and bimetallic nanocrystals with controlled particle size, high surface area, and more densely populated unsaturated surface coordination sites could potentially provide significantly improved catalytic performance over conventional catalysts.[63−70] Highly nonstoichiometric oxide nanoparticles such as CeO_{2-x} provide a high oxygen vacancy concentration and an active superoxide surface species.[63−66] These nanoparticle oxides enable catalytic activation at significantly lower temperatures for the reduction of sulfur dioxide and the oxidation of carbon monoxide.[63−70] Research in this area is motivated by the possibility of designing nanostructured catalysts that possess novel catalytic properties such as low temperature activity, selectivity, stability, and resistance to poisoning and degradation.[63−70] Such catalysts are essential for technological advances in environmental protection, improving indoor air quality, and chemical synthesis and processing. The low temperature oxidation of carbon monoxide is one of these important environmental issues since small exposure (ppm) to this odorless invisible gas can be lethal.[71] Therefore, the discovery that Au nanoparticles between 2 and 5 nm are exceptionally active for low temperature CO oxidation has stimulated extensive research to develop highly active catalysts to remove even a small amount of CO from the local environment.[72−76] There is also a strong incentive to develop active supported catalysts that utilize small amounts of the noble metals such as gold and palladium. The applications of bimetallic nanoalloys as supported catalysts could provide a wide range of activity and possible selectivity for CO oxidation reaction.

In this paper, we establish the MWI approach as a general procedure for the synthesis of a variety of high quality, crystalline bimetallic nanoalloys with controlled size and shape. The synthesis and characterization of bimetallic alloys of Au, Pt, and Pd with Ru, Rh, Ag, Cu, and Ni are reported. We also report the synthesis of selected nanoalloys supported on ceria nanoparticles as nanocatalysts for CO oxidation. This demonstrates another advantage of using the MWI approach where a supported nanoalloy catalyst can be prepared using a facile one-pot synthesis. The catalytic activities for the CO oxidation are presented and discussed. Our method could be expanded to prepare multimetallic nanoalloys with novel properties resulting from the different metallic properties coupled together in a single nanoalloy.

Experimental Section

Chemicals and Materials. Palladium(II) acetylacetonate ($Pd(acac)_2$, 99%), rhodium(III) acetylacetonate ($Rh(acac)_3$, 97%), copper(II) acetylacetonate ($Cu(acac)_2$, 99.99%), ruthenium(III) chloride ($RuCl_3$, Ru content 45−55%), platinum(IV) chloride ($PtCl_4$, 99.9+%), hydrogen tetrachloroaurate(III) ($HAuCl_4$, 30 wt % solution in dilute HCl), silver acetate (Agac, 99%), oleic acid (OAc, tech. 90%), oleylamine (OAm, tech. 70%), and *N*,*N*-dimethylformamide (DMF, 99.8%) were purchased from Sigma Aldrich. Nickel formate (99%) was purchased from Alfa Aesar. All chemicals were used without any further purification. Ethanol, dichloromethane, and toluene of analytical-reagent grade are used for all experiments.

Synthesis Procedure. In a typical reaction, metallic precursors of the selected alloy (1.45×10^{-4} mol of each metal) were dissolved in 1 mL of DMF before being injected in an equimolar mixture of liganding solvents of oleic acid, OA (0.114 mol), and oleylamine, OAm (0.114 mol). The mixture was kept in an oil bath under continuous stirring at a temperature of 110 °C using a stirring hot plate, until a clear solution was obtained. The clear solution was then placed in a conventional microwave set at 1000 W power and operated in 35 s cycles (on for 30 s, off and stirring for 5 s) for a total microwaving time that varied from 1 to 15 min (until the reaction mixture turned black). After cooling down, the bimetallic alloy nanocrystals were obtained by flocculating the reaction mixture in ethanol followed by particle separation using an Eppendorf 5804 centrifuge operated at 5000 rpm for 5 min. The particles were washed at least two times with ethanol and ethanol−toluene mixtures before being redispersed in 5 mL of toluene or dichloromethane. Table 1 lists the experimental conditions used in preparation of the different nanoalloys reported in this paper. It should be noted that the size of the nanocrystals is tuned by varying the concentration of the precursors and the MWI times, while the shape is controlled by varying the concentration and composition of the ligating solvents (oleic acid and oleylamine) which stabilize the nanocrystals by passivating the surfaces.

The syntheses of the nanocatalysts and the ceria nanoparticles support were carried out simultaneously in the same solution under the same experimental conditions. In this case, 0.5 g of cerium acetate was dissolved in an equimolar mixture of oleylamine and oleic acid first heated to about 110 °C in an oil bath to remove the hydrated water from the cerium acetate and obtain a clear solution. The metal precursors of the selected nanocatalyst alloy (equivalent to 5 wt % of the CeO_2) were dissolved in the above mixture until a clear solution was obtained (see Table 1 for specific experimental conditions). The clear solution was then placed in a conventional microwave set at 1000 W power and operated in 1−2 min cycles (on for 90 s, off and stirring for 30 s) for a total microwaving time that varied from 5 to 15 min. After cooling down, the bimetallic alloy supported on ceria nanocrystals were obtained by flocculating the reaction mixture in ethanol followed by particles' separation using an Eppendorf 5804 centrifuge operated at 5000 rpm for 5 min. The particles were washed at least two times with ethanol and ethanol−toluene mixtures before being calcinated in air at 500 °C in a muffle furnace.

Characterization. The X-ray diffraction (XRD) patterns of the powder samples were measured at room temperature with an X'Pert Philips Materials Research diffractometer, with Cu KαR

(63) Moser, W. R., Ed. Advanced Catalysts and Nanostructured Materials; Academic Press: New York, 1996.
(64) Henrich, V. E.; Cox, P. A. The Surface Science of Metal Oxides; Cambridge University Press: Cambridge, 1996.
(65) Chusuei, C. C.; Lai, X.; Luo, K.; Goodman, D. W. *Top. Catal.* **2001**, *14*, 71–83.
(66) Haruta, M.; Tsubota, S.; Kobayashi, T.; Kageyama, H.; Genet, M. J.; Delmon, B. *J. Catal.* **1993**, *144*, 175–192.
(67) Valden, M.; Lai, X.; Goodman, D. W. *Science* **1998**, *281*, 1647–1650.
(68) Choudhary, T. V.; Goodman, D. W. 2002, *21*, 25−34.
(69) Chou, K. C.; Markovic, N. M.; Kim, J.; Ross, P. N.; Somorjai, G. A. *J. Phys. Chem. B* **2003**, *107*, 1840–1844.
(70) Chen, M. S.; Goodman, D. W. *Science* **2004**, *306*, 252–255.
(71) World Health Organization. Carbon Monoxide: Environmental Health Criteria,; World Health Organization: Geneva, 1999; p 213.
(72) Haruta, M. *Catal. Today* **1997**, *36*, 153–166.
(73) Hutchings, G. J. *Gold Bull.* **1996**, *29*, 123–130.
(74) Hayashi, T.; Tanaka, K.; Haruta, M. *J. Catal.* **1998**, *178*, 566–575.
(75) Moreau, F.; Bond, G. C. *Catal. Today* **2006**, *114*, 362–368.
(76) Leff, D. V.; Brandt, L.; Heath, J. R. *Langmuir* **1996**, *12*, 4723–4730.

Table 1. Experimental Conditions for Preparing Organically Dispersible Nanoalloys

nanocrystals	precursors: OAm:OA (mole ratio)/MWI time	shape	average size (nm)
Pt	$PtCl_4$−OAm −OAc (1:60:30)/2 min	cubes	15
Pd	$Pd(acac)_2$−OAm−OAc (1:60:30)/10 min	cubes	10
Rh	$Rh(acac)_3$−OAm−OAc (1:60:30)/10 min	faceted particles	6
Ru	$RuCl_3$−OAm−OAc (1:60:30)/10 min	faceted fine particles	4
PtRh	$PtCl_4$−$Rh(acac)_3$−OAm−OAc (1:1:90:30)/5 min	distorted cubes	20−22
PtRu	$PtCl_4$−$RuCl_3$−OAm−OAc (1:1:90:30)/10 min	faceted fine structures	12
PdRh	$Pd(acac)_2$−$Rh(acac)_3$−OAm−OAc (1:1:90:30)/10 min	rod-like structures	12
PdRu	$Pd(acac)_2$−$RuCl_3$−OAm−OAc (1:1:90:30)/10 min	rod-like structures	15
Au	$HAuCl_4$−OAm−OAc (1:17:17)/1 min	spherical	10
Ag	Ag(ac)−OAm−OAc (1:8:8)/5 min	spherical	5
Cu	$Cu(ac)_2$−OAm−OAc (1:17:17)/8 min	hexagons	40−50
AuAg	$HAuCl_4$−Ag(ac)−OAm−OAc (1:1:34:34)/7 min	spherical	8
AgCu	Ag(ac)−$Cu(ac)_2$−OAm−OAc (1:1:8:8)/5 min	spherical	12
AuCu	$HAuCl_4$−$Cu(ac)_2$−OAm−OAc (1:2:67:42)/8 min	wire-like structures	10
Ni	$Ni(HCO_2)_2$−OAm−OAc (1:5:5)/15 min	hexagons	25−30
PtCu	$PtCl_4$−$Cu(ac)_2$−OAm−OAc (1:1:10:10)/3 min	spherical + elongated structures	12−15
PtAg	$PtCl_4$−Ag(ac)−OAm−OAc (1:1:10:10)/5 min	spherical	5
AuPd	$HAuCl_4$−$Pd(acac)_2$−OAm−OAc (1:1:10:10)/10 min	spherical + rod-like structures	6−8
AuPt	$HAuCl_4$−$PtCl_4$−OAm−OAc (1:1:10:10)/10 min	small hexagones	12
AuRu	$HAuCl_4$−$RuCl_3$−OAm−OAc (1:1:10:10)/10 min	spherical	10
AuRh	$HAuCl_4$−$Rh(acac)_3$−OAm−OAc (1:1:10:10)/10 min	spherical	12
PtPd	$PtCl_4$−$Pd(acac)_2$−OAm−OAc (1:1:10:10)/10	spherical	12
PdAg	$Pd(acac)_2$−Ag(ac)−OAm−OAc (1:1:10:10)/10 min	rod-like structures	15
PdCu	$Pd(acac)_2$−$Cu(ac)_2$−OAm−OAc (1:1:10:10)/10 min	spherical	5
PtNi	$PtCl_4$−$Ni(HCO_2)_2$−OAm−OAc (1:2:10:10)/15 min	spherical	12
PdNi	$Pd(acac)_2$−$Ni(HCO_2)_2$−OAm−OAc (1:2:10:10)/15 min	spherical	12
RuNi	$RuCl_3$−$Ni(HCO_2)_2$−OAm−OAc (1:2:10:10)/15 min	faceted	15

radiation. The optical absorption and the photoluminescence spectra for the toluene-dispersed core/shell nanocrystals were measured using HP-8453 spectrophotometer and Varian (CARY) Fluoro spectrometer, respectively. Transmission electron microscopy (TEM) was carried out using a Joel JEM-1230 electron microscope operated at 120 kV equipped with a Gatan UltraScan 4000SP 4K × 4K CCD camera. Samples for TEM were prepared by placing a droplet of colloid suspension in toluene on a Formvar carbon-coated, 300-mesh copper grid (Ted Pella) and allowing them to evaporate in air at room temperature. Additional TEM analyses were performed using a Joel 2010F field-emission gun operating at 200 kV and having an Oxford ultrathin window EDX detector. Scanning electron microscopy (SEM) and energy dispersive X-ray spectroscopy (EDX) were carried out using a Quantum DS-130S dual stage electron microscope. The X-ray photoelectron spectroscopy (XPS) analysis was performed on a Thermo Fisher Scientific ESCALAB 250 using a monochromatic Al Kα X-ray.

For the CO catalytic oxidation the sample was placed inside a Thermolyne 2100 programmable tube furnace reactor.[20] The sample temperature was measured by a thermocouple placed near the sample. In a typical experiment, a gas mixture consisting of 4 wt % CO and 20 wt % O_2 in helium was passed over the sample while the temperature was ramped. The gas mixture was set to flow over the sample at a rate of 100 cm^3/min controlled via MKS digital flow meters (Supporting Information). The conversion of CO to CO_2 was monitored using an infrared gas analyzer (ACS, Automated Custom Systems Inc.). All the catalytic activities were measured (using a 50 mg sample) after a heat treatment of the catalyst at 300 °C in the reactant gas mixture for 15 min to remove moisture and adsorbed impurities.

Results and Discussion

1. Synthesis and Characterization of the Metallic and Bimetallic Nanocrystals. The crystalline nature of the as-synthesized metallic and bimetallic nanoparticles was determined by X-ray diffraction measurements. The diffraction patterns of the pure metallic Au, Ag, Pd, Pt, Rh, Cu, and Ru nanoparticles are displayed in Figure 1. The measured patterns can be indexed to the [111], [200], [220], [311], and [222] planes of the face centered cubic (fcc) crystal structures for Au, Ag, Pd, Pt, Rh, and Cu nanoparticles. However, the Ru nanoparticles show a diffraction pattern that could be indexed to the [100], [101], [110], [103], and [201] planes of the hexagonal closed-packed (hcp) lattice, whereas the Ni nanoparticles show the presence of a major cubic crystalline phase with some traces of particles with hexagonal crystal structures (Figure S1, Supporting Information). The XRD results clearly indicate the absence of peaks that can be assigned to metal oxides. This is particularly important for the Cu and Ni nanoparticles where no oxidation by atmospheric oxygen was observed, thus, indicating the efficient surface capping and passivation by the oleic acid−oleyl amine mixture.

Parts a and b of Figure 2 displays the XRD patterns of the PtAu and PtRh (a) and CuAu and CuPt (b) nanoalloys, respectively. In comparing the XRD pattern of the nanoalloy to the patterns of the individual metals, it is clear that the diffraction peaks of the nanoalloy are located in between the corresponding peaks of the individual metals. This suggests the formation of a solid solution corresponding to the specific nanoalloy. The diffraction pattern of the nanoalloy is not simply a sum of the patterns of the individual components. The nanoalloy patterns also show no evidence of any pure metallic peaks which indicates that binary nucleation has been the major nucleation process involved in the formation of these alloys. Therefore, the absence of the diffraction peaks of the pure metal constituents and the appearance of new peaks located in between those of the pure metals provide strong evidence for the binary nucleation mechanism leading to the formation of

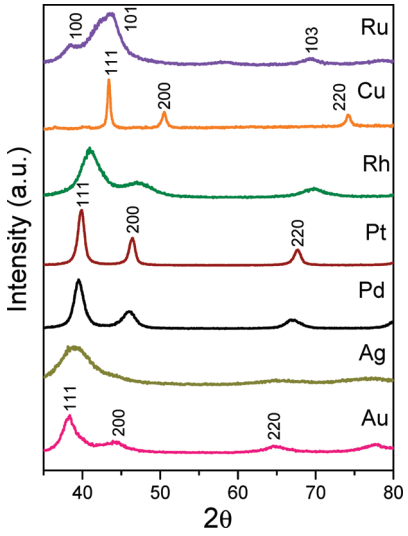

Figure 1. XRD patterns of metal nanocrystals prepared by the MWI method.

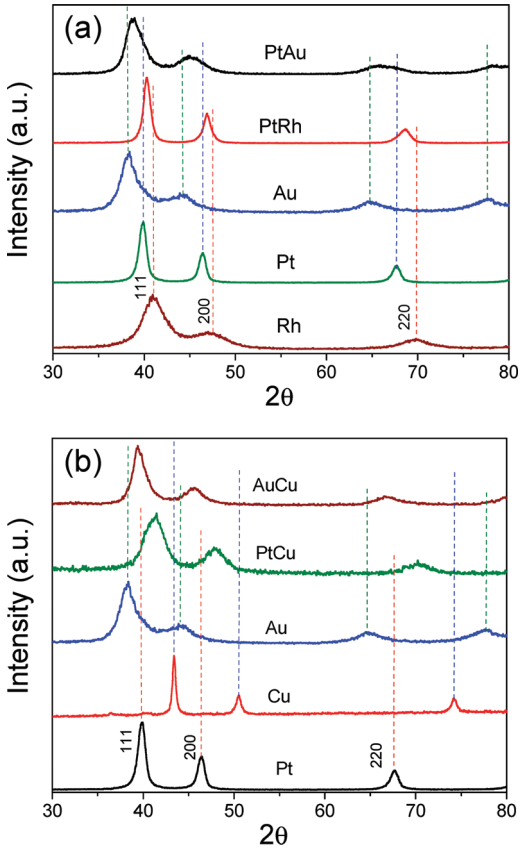

Figure 2. Comparisons of the XRD patterns of nanoalloys (a) PtAu and PtRh and (b) AuCu and PtCu, with the patterns of the individual metal nanocrystals prepared by the MWI method.

the alloyed nanocrystals. Similar results have been observed for other nanolloys such as RuPd, RuPt, AgAu, and AgPt as shown in Figures S2 and S3 (Supporting Information). It should be noted that the formation of nanoalloys among the Au, Ag, Pd, Pt, Rh, Cu, and Ru nanoparticles is thermodynamically favorable since these metals have the same fcc crystal structure with similar lattice constants. These alloys are likely to be formed by atom substitution of one metal for the other through

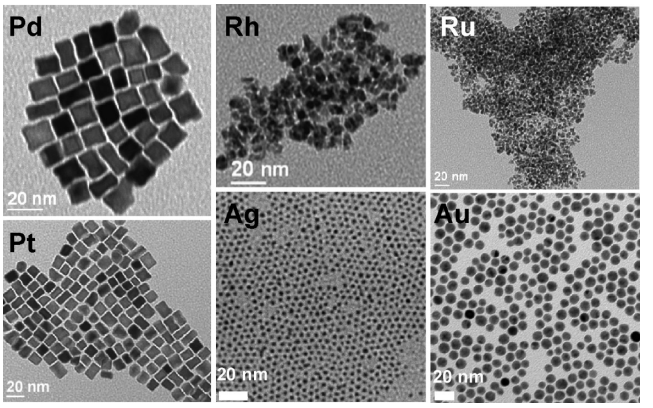

Figure 3. TEM images of metal nanocrystals prepared by the MWI method.

diffusion processes in the supersaturated solution of the binary metals or at the interfaces of the resulting nanocrystals. It is interesting, however, that the same trend of nanoalloy formation is also observed between Ru with the hcp lattice and the fcc metals such as Cu, Ag, Au, Pd, and Pt.

Figure 3 displays TEM images of the Au, Ag, Ru, Rh, Pt, and Pd nanocrystals prepared under the experimental conditions given in Table 1. By using a 1:1 ratio of OAm:OA, both Ag and Au produce monodispersed spherical nanocrystals with average diameters of 5 and 10 nm, respectively. The size of the particles can be controlled by varying the MWI time, the concentration of the metal precursor, and the OAm to OAc ratio. The metal ions in our experiments are reduced by the OAm which acts as both reducing agent and capping material as well. No nanoparticles are formed in pure OA even after MWI for several hours. This confirms that OAm is responsible for the reduction of metal ions and the formation of the metallic and bimetallic nanocrystals. However, the presence of OA clearly enhances the growth rate which could affect the final shape of the nanocrystal depending on the ratio of OAm:OA and MWI time. In the case of Ru and Rh, using a 2:1 ratio of OAm:OA produces small faceted nanocrystals with truncated prisms as the predominant shape of the nanocrystals as shown in Figure 3. The average particle size is 3−4 nm for Ru and 5−6 nm for Rh. Under similar conditions, both Pt and Pd nanocrystals form cubic shapes with an average edge of 15 and 10 nm, respectively. Similar Pt and FePt nanocubes have been prepared using a solvothermal method under nitrogen.[15,28]

Figure 4a shows TEM images of several examples of bimetallic nanoalloys. Most of the nanoalloys produced using a 1:1 ratio of OAm:OA show spherical particles. For the PdCu nanoalloy, very small spherical particles with an average diameter of less than 5 nm are formed. The particles are well dispersed with a narrow size distribution. For the PdAg nanoalloy, rod-like, 15−20 nm long nanocrystals are produced. Both the AuPd and the AuAg nanoalloys show spherical particles with an average particle size close to that of the pure Au nanocrystals. The PtRh nanoalloy shows deformed cubic shapes which seem to be a combination of the cubic shape Pt nanoparticles and the

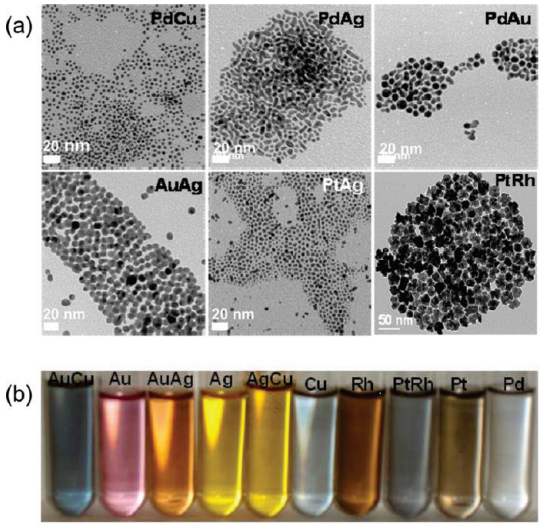

Figure 4. (a) TEM images of bimetallic nanoalloys prepared by the MWI method. (b) Digital photographs of metallic and bimetallic nanocrystals dispersed in toluene solutions.

faceted prism-like Rh particles. The average particle size of 20−25 nm of the PtRh nanoalloy is significantly larger than the size of the individual metal nanoparticles. All the nanoalloy solutions prepared by the MWI method and dispersed in toluene are very stable and can be stored for several months at room temperature without precipitation. This stability is due to the strong interaction between the OAm:OAc mixture and the surface of the bimetallic alloys which could form covalent-type interactions in some cases.[76] Figure 4b shows digital photographs of metallic nanocrystals and bimetallic nanoalloys dispersed in toluene solutions. The different colors of the nanoalloys as compared to the individual metals are clearly visible in all cases.

The EDX spectra of the PtCu, PtRh, PtRu, PtPd, PdAu, PdNi, PdRu, and PdCu nanoalloys confirm the presence of the corresponding metals in each nanoalloy as shown in Figure S4a−h, respectively (Supporting Information). The EDX spectra were measured on the Quantum DS-130S Dual Stage SEM using thin films of the prepared nanoalloys. The thin film was prepared by placing a few drops of the nanocrystals dispersed in a methylene chloride solution onto a clean aluminum holder. The holder was then placed in a desiccator at room temperature to dry into a thin film. The analysis of the EDX spectra reveals that the atomic ratios of the metal components in the nanoalloys do not change much from the starting ratios of the metal precursors. For example, the EDX spectrum of the PdCu nanocrystals indicates that the nanocrystals contain 49.4 atom % Pd and 50.6 atom % Cu, almost identical to the 1:1 ratio of the Pd and Cu precursors used in the synthesis. The insets shown in Figure S4a−h (Supporting Information) display the SEM images observed for different nanoalloys. It is clear that the nanoalloys exhibit very different morphologies and film porosities. The nanoalloy films of PtCu, PtRh, PdAu, and PdNi show less porous films while the nanoalloys of PdCu, PtRu, and PdRu show highly porous films. It is interesting that the PdCu nanoalloy with very small nanocrystals (5 nm) results in the formation of a highly porous film as shown in Figure S4h (Supporting Information). These films could have important applications for the selective adsorption of a variety of gases.

Further support for the formation of nanoalloys has been provided by high resolution TEM and NANO EDX analysis with a probe beam of 0.5 nm as shown in Figure 5 for the PtAu nanoalloy nanoparticles. The high resolution images show lattice fringes and structural defects such as stacking faults and twins that are often observed in nanoalloys.[4] This can be explained by the different growth rates of Pt on various planes of Au nanocrystals as well as by the anisotropy of the surface energy, which favors low-index [111] and [200] facets.[4] In the NANO EDX measurements, the electron beam was focused on a number of particles, as shown in the two examples given in Figure 5, and it was found that all particles consisted of Pt−Au alloy as evident from the corresponding EDX spectra. The average composition $Pt_{0.45}Au_{0.55}$ determined from the NANO EDX analysis is in excellent agreement with the SEM-EDX results and with the 1:1 atomic ratio of the Pt and Au precursors used in the synthesis.

Metallic nanoparticles exhibit unique optical properties due to their surface plasmon resonances (SPR), which result from the coherent collective oscillations of electrons in the conduction band of metal nanocrystals.[77,78] The optical properties of Au, Ag, Cu, Pd, Pt, Rh, and Ru nanoparticles dispersed in toluene have been investigated along with their bimetallic nanoalloys. Figure 6a shows the UV−Vis absorption spectra of Au, Ag, and AuAg nanocrystals. The Au and Ag particles show SPR absorptions at 530 and 428 nm, respectively. These values are red-shifted from the typical colloidal Au and Ag nanoparticles of the 6−8 nm size which have plasmon bands at about 520 and 380 nm, respectively.[77] The observed red shift could reflect the roles of OAm and OA in modifying the electronic structures of the Au and Ag nanocrystals. It has been shown that these capping molecules give rise to a shell of localized charge that modifies the refractive index of the medium surrounding the metallic core and reduces the size where the electrons can freely oscillate.[79] The optical absorption of the AuAg nanoalloy shows an SPR peak at 474 nm with no evidence for the SPR peaks of the individual Ag or Au nanocrystals. This SPR peak is similar to that observed for the $Au_{0.6}Ag_{0.4}$ alloy nanoparticles coated with oleylamine.[80] This result provides further evidence for the formation of the AuAg nanoalloy with a composition close to the 1:1 atomic ratio of the Au and Ag precursors used in the MWI synthesis.

Figure 6b shows the photoemissions observed from the Au, Ag, and AuAg nanocrystals. The photoemission in these metals is attributed to an interband recombination

(77) Hodak, J. H.; Henglein, A.; Giersig, M.; Hartland, G. V. *J. Phys. Chem. B* **2000**, *104*, 11708–11718.
(78) Kariuki, N. N.; Luo, J.; Maye, M. M.; Hassan, S. A.; Menard, T.; Naslund, H. R.; Lin, Y.; Wang, C.; Engelhard, M. H.; Zhong, C. J. *Langmuir* **2004**, *20*, 11240–11246.
(79) de la Presa, P.; Multigner, M.; de la Venta, J.; Garcia, M. A.; Ruiz-Gonzalez, M. L. *J. Appl. Phys.* **2006**, *100*, 123915/1–123915/6.
(80) Wang, C.; Yin, H.; Chan, R.; Peng, S.; Dai, S.; Sun, S. *Chem. Mater.* **2009**, *21*, 433–435.

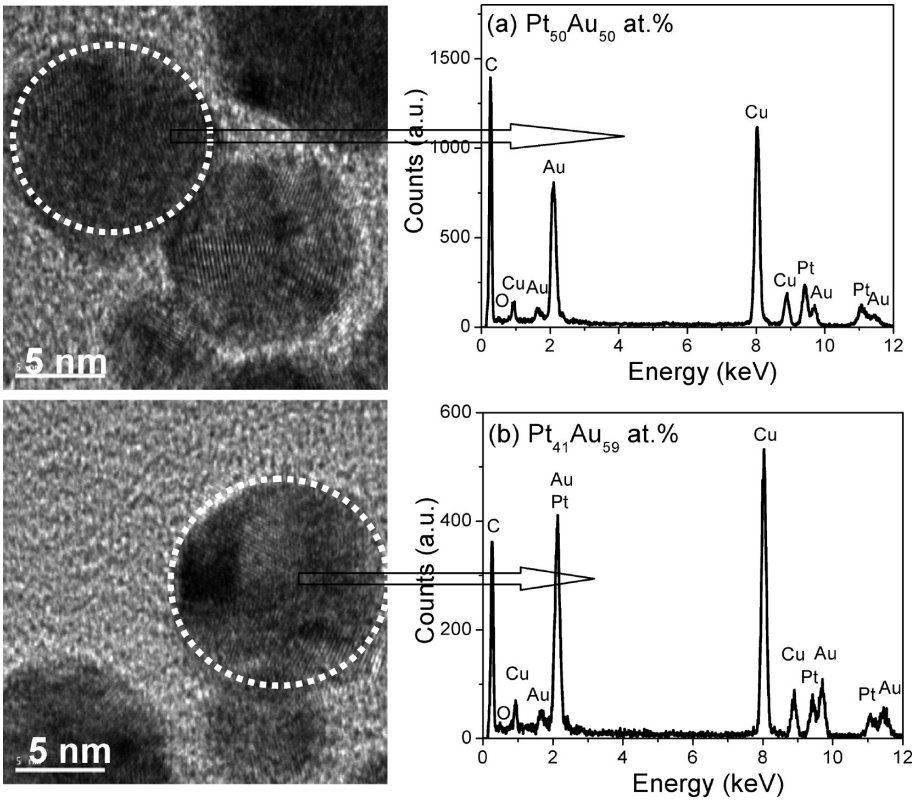

Figure 5. High resolution TEM images of PtAu nanoalloy and NANO EDX spectra of two different particles showing atomic percent compositions of 50% Pt, 50% Au (top) and 41% Pt, 59% Au (bottom).

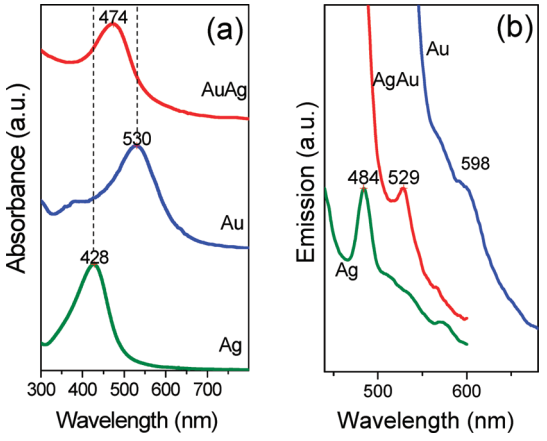

Figure 6. (a) UV−Vis absorption spectra of Ag, Au, and AuAg nanocrystals in toluene. (b) Photoemission spectra of Ag, Au, and AuAg nanocrystals.

between electrons and holes. The Ag, AgAu, and Au nanocrystals exhibit emission peaks at 484, 529, and 598 nm, respectively. It is clear that all emission peaks are red-shifted in comparison to the SPR peaks observed in Figure 6a. Also the alloy nanocrystals were found to emit between the emission wavelengths of pure Ag and Au nanocrystals. The absorption and emission spectra show that the AgAu alloy particles have optical properties different from that of Ag or Au particles and could be tuned under an excitation or emission mode that depends on the alloy composition. The intensity of the photoemission peaks was found to decrease from Ag > AgAu > Au as the Au nanocrystals have a very small quantum yield.[81,82]

The absorption and fluorescence spectra of the PdCu, PdAu, and AdAg nanoalloys are displayed in Figure 7a,b. The absorption spectra (Figure 7a) show the absence of any SPR peaks corresponding to Ag, Au, or Cu metal indicating the absence of any pure metal nanoparticles and hence suggesting the formation of nanoalloys. This result is similar to that reported by other groups.[83] On the other hand, the fluorescence spectra show that the emission peaks are shifted to the red as the Pd-conjugate metal changes from Ag (473 nm) to Au (532 nm) to Cu (558 nm).

2. CO Oxidation on Ceria Supported Bimetallic Nanoalloys. In this section, we investigate the catalytic activity for CO oxidation of the metallic and bimetallic nanocrystals supported on CeO_2 nanoparticles prepared using the MWI approach. In all cases, samples of 5 wt % nanocatalyst supported on CeO_2 nanoparticles were considered. In these syntheses, the shape control of the supported nanocatalysts was not clearly observed probably because of the small concentration of the metallic and bimetallic nanoparticles relative to the CeO_2 nanoparticles. Also, because of the removal of the capping agents through the calcination process, the metallic nanoparticles are not expected to retain their original shapes produced by the synthesis. The only exception among the synthesized supported nanoparticles was Pd/CeO_2 nanoparticles which

(81) Mooradian, A. *Phys. Rev. Lett.* **1969**, *22*, 185–187.
(82) Mohamed, M. B.; Volkov, V.; Link, S.; El-Sayed, M. A. *Chem. Phys. Lett.* **2000**, *317*, 517–523.
(83) Toshima, N.; Yonezawa, T. *New J. Chem.* **1998**, *22*, 1179–1201.

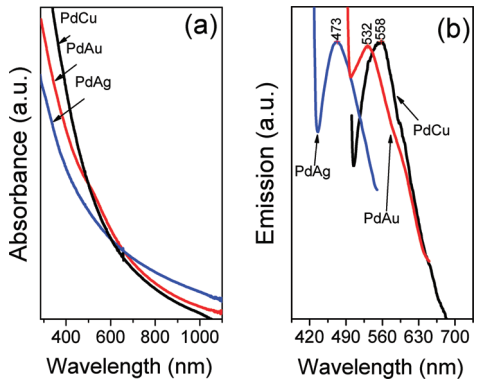

Figure 7. (a) UV−vis absorption spectra of PdCu, PdAu, and PdAg nanocrystals. (b) Photoemission spectra of PdCu, PdAu ,and PdAg nanocrystals.

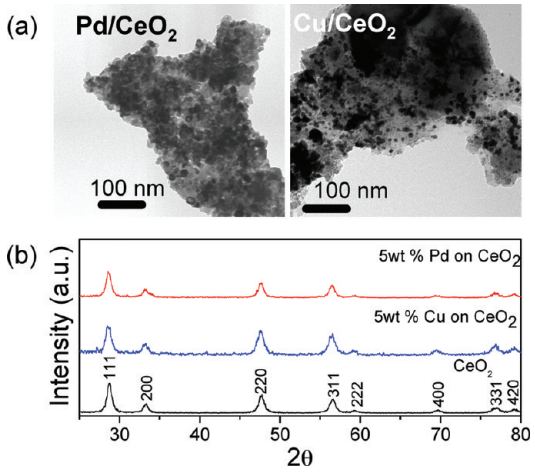

Figure 8. (a) TEM images of 5 wt % Pd/Ceria and Cu/ceria nanoparticles prepared by the MWI method following the calcinations of the samples in air at 500 °C. (b) Comparisons of the XRD patterns of CeO_2, 5 wt % Pd/ CeO_2, and 5 wt % Cu/ CeO_2 prepared by the MWI method.

appeared to retain their cubic shape even after calcination. Figure 8a displays representative examples of TEM images of the 5 wt % samples of the Pd/CeO_2 and Cu/CeO_2 nanocatalysts following the calcination of the samples in air at 500 °C. The TEM images show that the Pd and Cu nanoparticles are well dispersed within the CeO_2 nanoparticles with no evidence for aggregation. This is also supported by comparing the XRD pattern of pure CeO_2 nanoparticles with patterns of the two nanocatalysts consisting of 5 wt % Cu and 5 wt % Pd supported on CeO_2 nanoparticles as shown in Figure 8b. It is clear that all the three patterns match well with CeO_2 (ICCD 00-034-0394) from the database with no evidence of Pd or Cu peaks. This provides further support for the dispersion of the small Pd and Cu nanoparticles within the ceria support. Volume-weighted average crystalline size of the ceria nanoparticles calculated from the XRD peak width using Scherrer's equation indicates that the average particle size is about 5 nm.[84] This size is smaller than that observed from TEM due to the polycrystalline nature of the nanoparticles. Also, because of the high contrast from the Pd or Cu nanoparticles, the individual cerium oxide nanoparticles are not clearly shown in the TEM images shown in Figure 8a.

(84) Klug, H. P.; Alexander, L. E. X-ray Diffraction Procedures for Polycrystalline and Amorphous Materials, 2nd ed.; Wiley: New York, 1974.

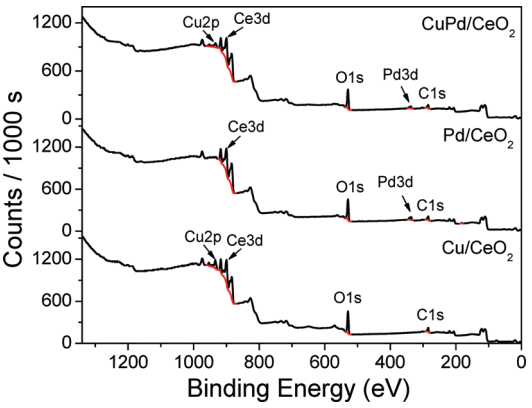

Figure 9. XPS survey spectra of 5 wt % Cu, 5 wt % Pd, and 5 wt % CuPd nanoalloy supported on CeO_2 nanoparticles.

To characterize the surface composition of the supported nanocatalysts, we carried out XPS measurements on several metallic and bimetallic catalysts supported on CeO_2 nanoparticles. Figure 9 displays the XPS survey scans of the Cu/CeO_2, Pd/CeO_2 and CuPd/CeO_2 nanocatalysts. It is clear the spectrum of the bimetallic catalyst reveals the presence of both Cu and Pd on the surface layers of the nanoparticles. However, the surface composition is somewhat different from the particle's composition used in the MWI synthesis. For example, the surface compositions of the prepared 5 wt % Cu/CeO_2 and 5 wt % Pd/CeO_2 nanoparticles were found to contain 10 wt % Cu and 2 wt % Pd, respectively. Similarly, the prepared 5 wt % CuPd/CeO_2 nanoparticles were found to contain 6.8 wt % Cu and 3.5 wt % Pd at the surface. The tendency for excess surface enrichment of Cu could be related to lowering the surface free energy of the bimetallic nanoparticle. Detailed XPS studies of the bimetallic nanoalloys are currently under investigation in our laboratory.

Figure 10 compares the CO conversions over different 5 wt % metallic nanocatalysts supported on ceria prepared by the MWI method. It is clear that the Pd sample exhibits the highest activity with 50% and 96% conversions of CO to CO_2 at temperatures of 63 and 91 °C, respectively (Table 2). The performance of this catalyst is significantly improved over the 5 wt % Pd nanoparticles supported on ceria nanoparticles prepared previously using MWI but without the use of OAm−OAc as the reducing and capping agent.[45] In that work, the Pd/ceria catalyst was prepared in an aqueous medium using NaOH with no capping agents added. The resulting catalyst showed 50% and 100% conversions of CO to CO_2 at temperatures of 140 and 151 °C, respectively.[45] In the present work, the use of an OAm−OAc mixture resulted in the formation of cubic shaped well-dispersed nanocrystals which remained well-dispersed within the ceria nanoparticles even after the heat treatment at 500 °C to remove the organic materials as shown in the TEM of Figure 8a. The performance of the Pd/ceria nanocatalyst shown in Figure 10 is also much better than the Pd/ceria catalyst reported in ref 85 where the 100% CO conversion was reported to occur at ~220 °C

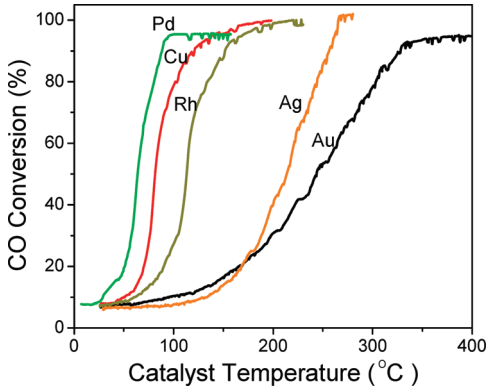

Figure 10. CO oxidation on different metal/CeO_2 nanoparticles prepared by the MWI method.

Table 2. Temperatures for the CO Oxidation (3%, 50% and max % conversion) over Nanocatalysts Supported on Ceria Nanoparticles Synthesized by the MWI Method

	$T_{3\%}$ (°C)	$T_{50\%}$ (°C)	% max (T, °C)
		Metals	
Pd	29	63	96% (91)
Cu	52	82	95% (140)
Rh	62	113	100% (202)
Au	98	243	92% (327)
Ag	115	214	100% (266)
Pt	218	286	100% (306)
		Alloys	
PdCu	44	74	94% (86)
PdPt	37	78	91% (152)
CuRh	57	95	96% (158)
AuPd	63	115	93% (186)
PdAg	47	78	94% (174)
RhAg	56	107	100% (197)
RhPt	93	155	100% (217)
CuPt	76	102	92% (221)
AuPt	159	225	94% (236)
PdRh	116	178	98% (227)
AuRh	136	83	96% (230)
CuAg	66	99	100% (284)
AuCu	110	303	81% (420)

following the heat treatment of the catalyst.[85] Other ceria-supported nanocatalysts which exhibited reasonable activity for the CO oxidation are the 5 wt % Cu and Rh catalysts as shown in Figure 10. Again, the TEM images of these catalysts obtained after the heat treatment at 500 °C show well-dispersed particles within the ceria support. On the other hand, the activity of the current 5 wt % Au/ceria catalyst is significantly lower (50% and 92% CO conversions at 243 and 327 °C, respectively) than the previously prepared
5 wt % Au/ceria catalyst synthesized in aqueous medium in the absence of capping agents (50% and 93% CO conversions at 67 and 211 °C, respectively).[45] However, the performance of the current Au/ceria catalyst is similar to other Au/ceria catalysts where 50% and 90% CO conversions were reported to occur at 272 and 380 °C, respectively following the calcination of the catalyst at 500 °C.[86]

(85) Zhu, H.; Qin, Z.; Shan, W.; Shen, W.; Wang, J. *Catal. Today* **2007**, *126*, 382–386.
(86) Russo, N.; Fino, D.; Saracco, G.; Specchia, V. *Catal. Today* **2006**, *117*, 214–219.

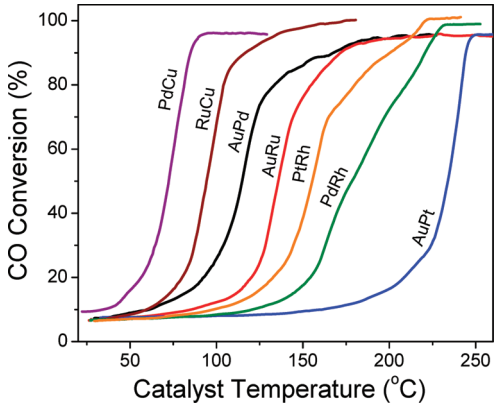

Figure 11. CO oxidation on different bimetallic nanoalloys supported on CeO_2 nanoparticles.

This can be attributed to the aggregation of the Au nanoparticles following the removal of the capping materials by the heat treatment at 500 °C. The fact that the Pd and Cu catalysts did not exhibit low activity following the same heat treatment at 500 °C implies that the tendency for aggregation of these nanoparticles is probably less than that of Au.

It should be noted that the catalytic activity of the present nanoparticle catalysts supported on ceria is strongly dependent on the removal of the organic capping materials. Incomplete removal of the organic materials leads to poor catalytic activity and rapid deactivation of the catalyst.

Figure 11 compares the activity of several nanoalloys supported on ceria toward CO oxidation. The performance of the supported bimetallic alloys is consistent with observed activity of the supported metal catalysts shown in Figure 10. For example, the highest activity is observed for the Pd, Cu, and Rd-containing nanoalloys according to the order CuPd > CuRh > AuPd > AuRh > PtRh > PdRh > AuPt. Both the CuPd and CuRh supported nanoalloys show promising results as efficient CO oxidation catalysts with 50% conversions at 74 and 95 °C, respectively. The highest conversions for these catalysts were 94% and 96% observed at 86 and 158 °C, respectively. For the PdAu nanoalloy supported on ceria, 50% and 93% conversions were observed at 115 and 186 °C, respectively. This is significantly better than the activity of bimetallic PdAu nanoalloy supported on TiO_2 nanoparticles where the 1% and 100% CO conversions were reported to occur at 150 and 250 °C, respectively.[87] The activity of the PdAu nanoalloy supported on ceria is also much higher than that of Au supported on ceria (50% and 92% CO conversions at 243 and 327 °C, respectively). This indicates that the catalytic activity of Au for CO oxidation can be enhanced by alloying with Pd. This is also consistent with similar findings for the alloying of Au with Ag.[80] The catalytic activity of the prepared supported nanoalloys can be further enhanced by optimizing the MWI synthesis method and the heat treatment of the catalysts. The main objective of the present work was to demonstrate the one-step

(87) Scott, R. W. J.; Sivadinarayana, C.; Wilson, O. M.; Yan, Z.; Goodman, D. W.; Crooks, R. M. *J. Am. Chem. Soc.* **2005**, *127*, 1380–1381.

synthesis of supported nanoalloys and to establish their application in nanocatalysis. Future work will focus on tuning the size, shape and composition through the MWI synthesis of selected promising nanoalloy catalysts such as CuPd, CuRh, and AuPd to enhance their activities.

Conclusions

In conclusion, the microwave irradiation method is simple, versatile, and rapid. It allows the synthesis of a wide variety of bimetallic nanoalloys with controlled size and shape. The important advantage of microwave dielectric heating over convective heating is that the reactants can be added at room temperature (or slightly higher temperatures) without the need for high-temperature injection. Furthermore, the same method can be used to synthesize bimetallic nanoalloys supported on ceria nanoparticles as nanocatalysts for CO oxidation. The current results reveal that the CuPd, CuRh, and AuPd supported nanoalloys exhibit high activity for CO oxidation. Optimizations of the size, composition, and shape of these nanoalloys could provide a new family of highly efficient bimetallic nanocatalysts for the low temperature oxidation of CO.

Acknowledgment. We thank the NSF (CHE-0414613 and CHE-0820945 to VCU) and NASA (NNX08AI46G to VCU) for the support of this work.

Supporting Information Available: XRD data for Ni, Pt, Ru, Pd, Au, and Ag nanocrystals; XRD data for PdNi, PtNi, RuNi, PtRu, PdRu, AuAg and PtAg nanoalloys; EDX data for PtCu, PtRh, PtRu, PtPd, PdAu, PdNi, PdRu, and PdCu nanoalloys; and experimental setup for the CO oxidation on nanoparticles (PDF). This material is available free of charge via the Internet at http://pubs.acs.org.